Supplementary information

for

Importance of the catalyst–water Coulomb interaction for oxygen reduction reaction kinetics

Teng Liu, Yinghe Zhao* and Tianyou Zhai*

State Key Laboratory of Materials Processing and Die & Mould Technology, School of Materials Science and Engineering, Huazhong University of Science and Technology, Wuhan 430074, China

*E-mail: zhaoyh@hust.edu.cn; zhaity@hust.edu.cn

Note S1. Fig. S1a presents the initial structure of the Pt/water interface. The flat bilayer ice structure of water at the interface was constructed by reference to the study by Ogasawara et al.[1] The water molecules in a disordered arrangement above the flat bilayer ice structure were generated by the genbox tool of the GROMACS software. Fig. S1b presents the representative equilibrium AIMD (ab-initio molecular dynamics) simulation snapshot. The statistical results of the distribution of water molecules near Pt at 298.15 K are shown by the red curve in Fig. S1c. Our statistical results agree well with Groß et al.[2] The statistical results from the MD simulation with UFF parameters are shown by the black curve in Fig. S1c. From comparison of red and black curves, it can be concluded that the simulation based on UFF parameters cannot well capture the main features of the distribution profile from the AIMD simulation. For example, there is a very obvious peak in the red curve, whereas the corresponding peak is not very obvious in the black curve. It is therefore necessary to further validate whether the conclusions based on UFF are reliable. To this end, we made new forcefield parameters by fitting the AIMD simulation results (the new force field is available from GitHub at https://github.com/yhzhao1989/New-FF). The blue curve in Fig. S1c shows the distribution from the MD simulation with new parameters. A very obvious peak can be observed in the blue curve. Importantly, the conclusions based on new parameters are consistent with those based on UFF parameters: first, although the O_2(interface) concentration decreases from 5.87×10^{-1} to 4.15×10^{-1}, it is still significantly larger than the O_2(interface) concentrations of TMOs (Fig. S2); second, the Pt–water Coulomb interaction is still significantly weaker than the TMO–water Coulomb interactions (Fig. S2); third, and most importantly, the simulated polarization curve representing the ORR kinetics of Pt changes very little (*e.g.*, the half-wave potential $E_{1/2}$ only changes slightly from 0.87 V to 0.86 V, as shown in Fig. S3) and still shows good agreement with the experimental result.[3] Overall, by comparing the conclusions based on UFF parameters with those based on new forcefield parameters (which were obtained by fitting the AIMD simulation results), it can be concluded that MD with UFF is valid to learn the Pt/water interface. Next, we focus on proving the validity of the MD simulation with UFF for learning the TMO/water interface. Fig. S4a and S5a present the initial structures. The water molecules in a disordered arrangement were generated by the genbox tool of the GROMACS software. Fig. S4b and S5b present the representative equilibrium AIMD simulation snapshots. The statistical results of the distributions of water molecules near TMOs at 298.15 K are shown by red curves in Fig. S4c and S5c. Black curves in Fig. S4c and S5c show the statistical results from the MD simulations with UFF parameters. The MD simulations based on UFF can well capture the main features of the distribution profiles from the AIMD simulations, as shown in Fig. S4c and S5c. For example, two very obvious peaks and a deep valley between two peaks can be observed within 0.5 nm in both red and black curves. Therefore, MD with UFF is also valid to learn the TMO/water interface.

Note S2. Pt is a typical noble metal, and $HfO_2(111)$ and $ZrO_2(111)$ belong to the family of TMOs. Consequently, it is interesting to validate whether transitional and noble metals exhibit similar catalyst–water Coulomb interactions and transitional and noble metal oxides (NMOs) exhibit similar catalyst–water Coulomb interactions. Five metals are used here to validate whether transitional and noble metals exhibit similar catalyst–water Coulomb interactions. Specifically, besides Pt(111), we also calculated the catalyst–water Coulomb interactions of four other metals (Ni, Cu, Ag, and Au). The four metals are all commonly used in heterogeneous electrocatalysis. Ni is an excellent electrocatalyst for hydrogen oxidation,[4] and Cu, Ag, and Au are commonly used to catalyse electrochemical CO_2 reduction.[5–7] The most energetically stable facet was chosen as the representative for validation. The (111) facet is the most energetically stable facet for all four metals. From the results in Table S4, it can be concluded that similar to noble metals, transitional metals also exhibit a significantly weaker catalyst–water interaction compared with transitional and noble metal oxides. Five metal oxides are used here to validate whether transitional and noble metal oxides exhibit similar catalyst–water Coulomb interactions. Specifically, besides $HfO_2(111)$ and $ZrO_2(111)$, we also calculated the catalyst–water Coulomb interactions of three other metal dioxides (RuO_2, IrO_2, and MnO_2). The three metal dioxides are all commonly used in heterogeneous electrocatalysis—they are excellent electrocatalysts for water oxidation.[8–10] The most energetically stable facet was chosen as the representative for validation. The (110) facet is the most energetically stable facet for all three metal dioxides. From the results in Table S4, it can be concluded that similar to transitional metal oxides, noble metal oxides also exhibit a significantly stronger catalyst–water Coulomb interaction compared with transitional and noble metals.

Note S3. The high-throughput experimental study by Nørskov et al. reveals the limited ORR kinetic performance of TMOs.[11] By taking $HfO_2(111)$ and $ZrO_2(111)$ as models and comparing with $Pt(111)$, our calculations revealed that the low O_2(interface) concentration is an important factor leading to the limited ORR kinetic performance of TMOs. Our calculations further showed that the reason behind the low O_2(interface) concentration lies in the strong catalyst–water Coulomb interaction. Apart from $HfO_2(111)$ and $ZrO_2(111)$, Nørskov et al. provided the atomic coordinates of 30 TMOs. We calculated the O_2(interface) concentrations and catalyst–water Coulomb interactions of all 30 TMOs based on the coordinates that they provided (Table S8). As revealed by the microkinetic analysis based on $Pt(111)$ (Fig. S14a), the half-wave potential is below 0.80 V when the O_2(interface) concentration falls beneath 0.1 c_{Pt}; the diffusion-limiting current density begins to decrease dramatically once the O_2(interface) concentration is below 0.1 c_{Pt}. These results mean that materials with an O_2(interface) concentration of less than 0.1 c_{Pt} encounter difficulty in becoming an excellent ORR electrocatalyst, even if they are endowed with comparable ORR activity to $Pt(111)$. Consistent with $HfO_2(111)$ and $ZrO_2(111)$, all 30 TMOs have an O_2(interface) concentration of less than 0.1 c_{Pt} (Fig. S14b), which supports the conclusion that the low O_2(interface) concentration is an important factor leading to the limited ORR kinetic performance of TMOs. Also consistent with $HfO_2(111)$ and $ZrO_2(111)$, all 30 TMOs have a significantly stronger catalyst–water Coulomb interaction compared with $Pt(111)$ (Table S8). Remarkably, when not considering the catalyst–water Coulomb interactions in the simulations, all 30 TMOs experience a marked increase in the O_2(interface) concentration and their O_2(interface) concentrations are able to exceed 0.1 c_{Pt} (Table S8), which unambiguously shows that the reason behind the low O_2(interface) concentration lies in the strong catalyst–water Coulomb interaction.

Note S4. Fig. S25 presents the free energy profiles for the dissociation of the product water from the Pt site under different water wall conditions. It emerges from the results in Fig. S25 that the water wall also affects the water dissociation—a stronger water wall renders the water dissociation more difficult. To further explore the effect of the water dissociation on the catalytic performance, we incorporated the water dissociation step into the microkinetic model. Accordingly, Fig. S26a presents the calculated polarization curves representing ORR kinetic performance under different water wall conditions. The half-wave potentials derived from the polarization curves are shown in Fig. S26b. Besides, Fig. S26b further compares the half-wave potentials in the absence and presence of water dissociation effect. The comparison unambiguously shows that the effect arising from the water dissociation becomes increasingly evident as the water wall strengthens. Remarkably, the fundamental conclusion of this work is that a stronger catalyst–water Coulomb interaction leads to a stronger water wall, thereby resulting in a poorer kinetic performance. Importantly, factoring in the water dissociation effect not only does not undermine our conclusion, but also further strengthens it. In addition, it is worth emphasizing that the effect resulting from the water dissociation is relatively weaker than that caused by the O_2 penetration.
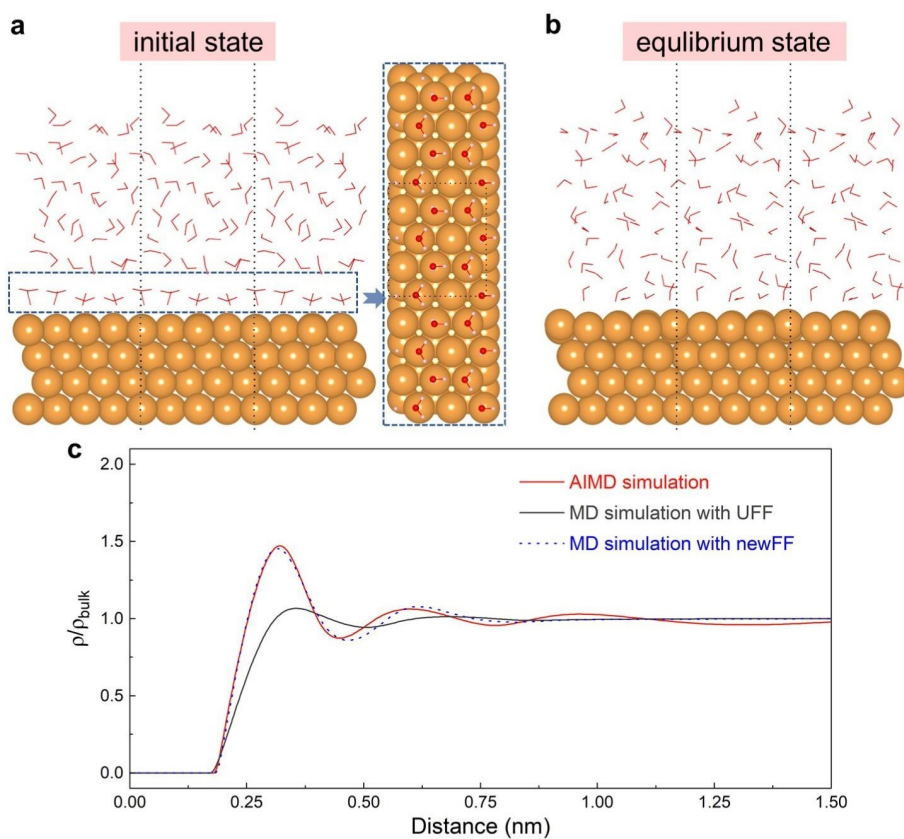
Fig. S1 (a) Snapshot of the initial Pt(111)/water interface, along with the top view of the flat bilayer ice structure of water at the interface. (b) Representative AIMD simulation snapshot of the Pt(111)/water interface at equilibrium at 298.15 K. The simulation box is repeated periodically to exhibit the boundary of the simulation box more clearly. The black dash lines denote the boundary of the box. (c) Distributions of water molecules near Pt at 298.15 K. ρ_{bulk} represents the water density in bulk water. The red curve indicates the distribution from the AIMD simulation, the black curve indicates the distribution from the MD simulation with UFF parameters, and the blue curve indicates the distribution from the MD simulation with new forcefield parameters (newFF).
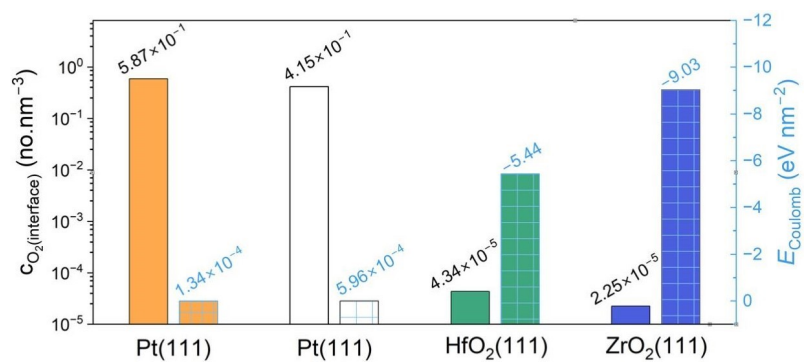
Fig. S2 O_2(interface) concentrations and catalyst–water Coulomb interactions of Pt(111), HfO$_2$(111), and ZrO$_2$(111). Empty bars denote the results from the MD simulation with new forcefield parameters. Shadowed bars denote the results from the MD simulation with UFF parameters.
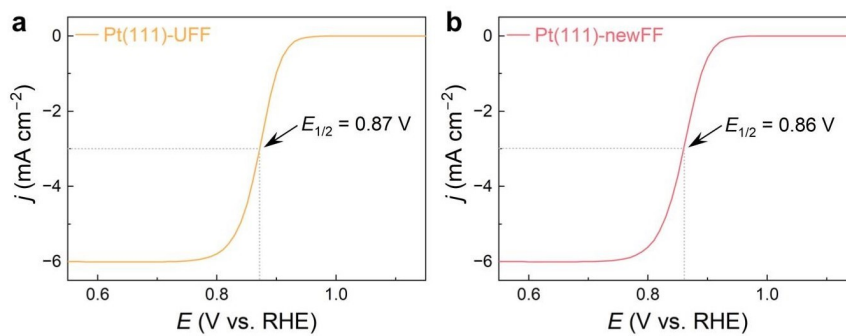
Fig. S3 Simulated polarization curves of Pt(111). The O_2(interface) concentration for the polarization curve calculation is obtained by (a) the MD simulation with UFF parameters and (b) the MD simulation with new forcefield parameters (newFF).

Fig. S4 (a) Snapshot of the initial HfO$_2$(111)/water interface. (b) Representative AIMD simulation snapshot of the HfO$_2$(111)/water interface at equilibrium at 298.15 K. The simulation box is repeated periodically to exhibit the boundary of the simulation box more clearly. The black dash lines denote the boundary of the box. (c) Distributions of water molecules near HfO$_2$ at 298.15 K. ρ_{bulk} represents the water density in bulk water. The red curve indicates the distribution from the AIMD simulation and the black curve indicates the distribution from the MD simulation with UFF parameters.

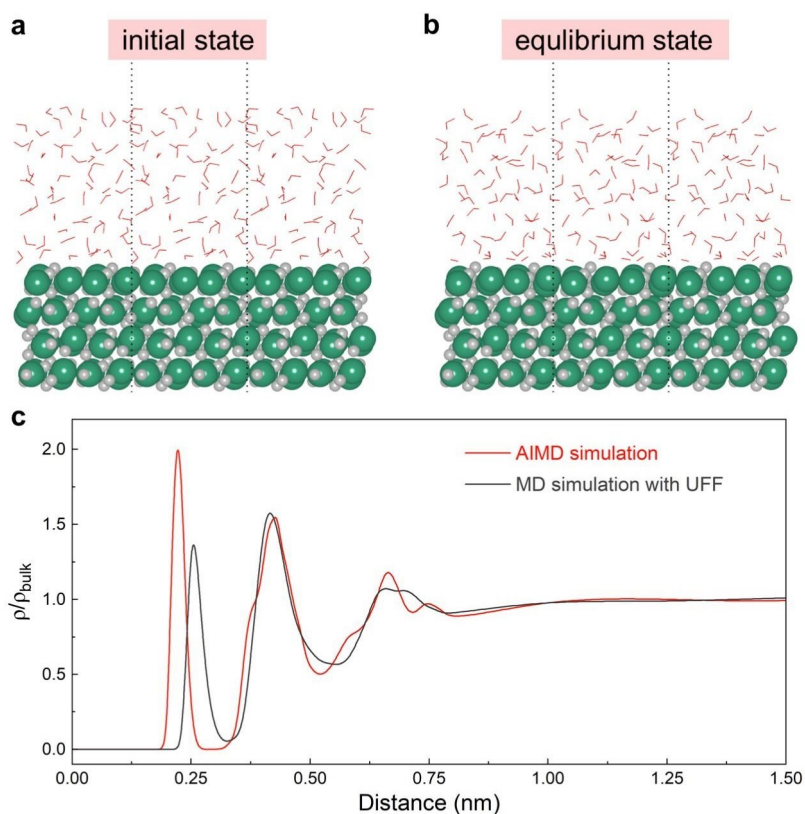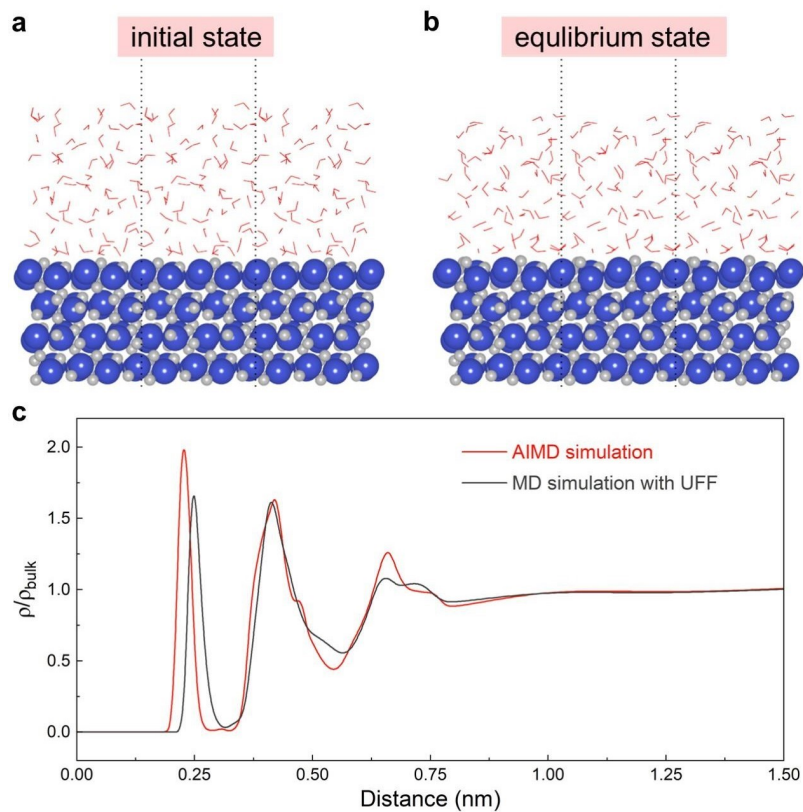**Fig. S5** (a) Snapshot of the initial $ZrO_2(111)$/water interface. (b) Representative AIMD simulation snapshot of the $ZrO_2(111)$/water interface at equilibrium at 298.15 K. The simulation box is repeated periodically to exhibit the boundary of the simulation box more clearly. The black dash lines denote the boundary of the box. (c) Distributions of water molecules near ZrO_2 at 298.15 K. ρ_{bulk} represents the water density in bulk water. The red curve indicates the distribution from the AIMD simulation and the black curve indicates the distribution from the MD simulation with UFF parameters.
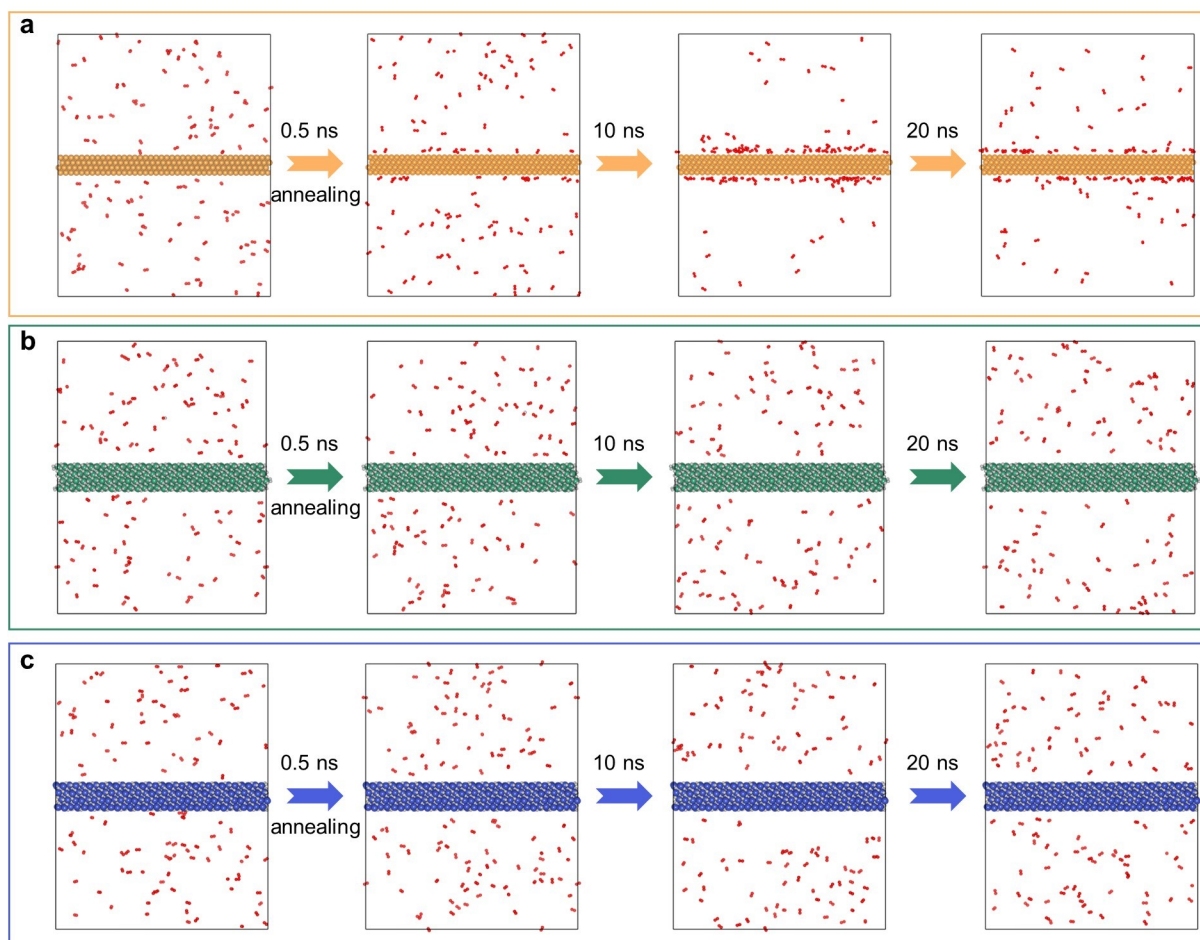
Fig. S6 Evolution processes of the distributions of O_2 molecules on the catalysts in water. The catalysts in (a)–(c) are Pt(111), HfO_2(111), and ZrO_2(111), respectively. Orange, green, and blue balls represent Pt, Hf, and Zr atoms, respectively. The O atoms of O_2 molecules and the O atoms of HfO_2 and ZrO_2 are denoted by red and grey balls, respectively. H_2O molecules are not displayed to clearly show the distributions of O_2 molecules.

Fig. S7 Representative equilibrium simulation snapshots of studied multiphase models. The multiphase models consist of catalysts, O_2 molecules, and water. The catalysts in (a)–(c) are Pt(111), HfO_2(111), and ZrO_2(111), respectively. Orange, green, and blue balls represent Pt, Hf, and Zr atoms, respectively. The O atoms of O_2 molecules and the O atoms of HfO_2 and ZrO_2 are denoted by red and grey balls, respectively. H_2O molecules are displayed in the line mode.
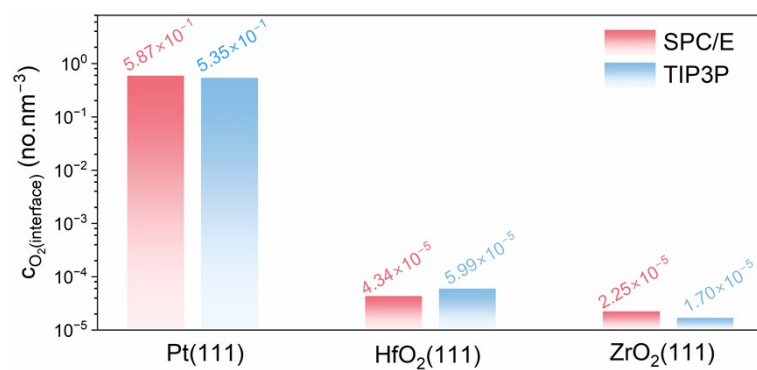
Fig. S8 O_2(interface) concentrations of Pt, HfO_2, and ZrO_2. Red and blue bars indicate the SPC/E and TIP3P model results, respectively.

Fig. S9 Distributions of O_2 molecules at the catalyst/water interfaces. (a) Representative equilibrium simulation snapshots of studied multiphase models. The multiphase models consist of catalysts, O_2 molecules, and water. The catalysts from left to right are Pt(111), HfO_2(111), and ZrO_2(111). Orange, green, and blue balls represent Pt, Hf, and Zr atoms, respectively. The O atoms of O_2 molecules and the O atoms of HfO_2 and ZrO_2 are denoted by red and grey balls, respectively. H_2O molecules are not displayed to clearly show the distributions of O_2 molecules. (b) Number densities of O_2 molecules near catalyst surfaces. z = 0 represents the position of the catalytic site at the interface. (c) O_2(interface) concentrations and catalyst–water Coulomb interactions corresponding to the three systems. The O_2 concentration of the simulated system is about 100 times higher than the saturating concentration at atmospheric pressure and room temperature (298.15 K).

14
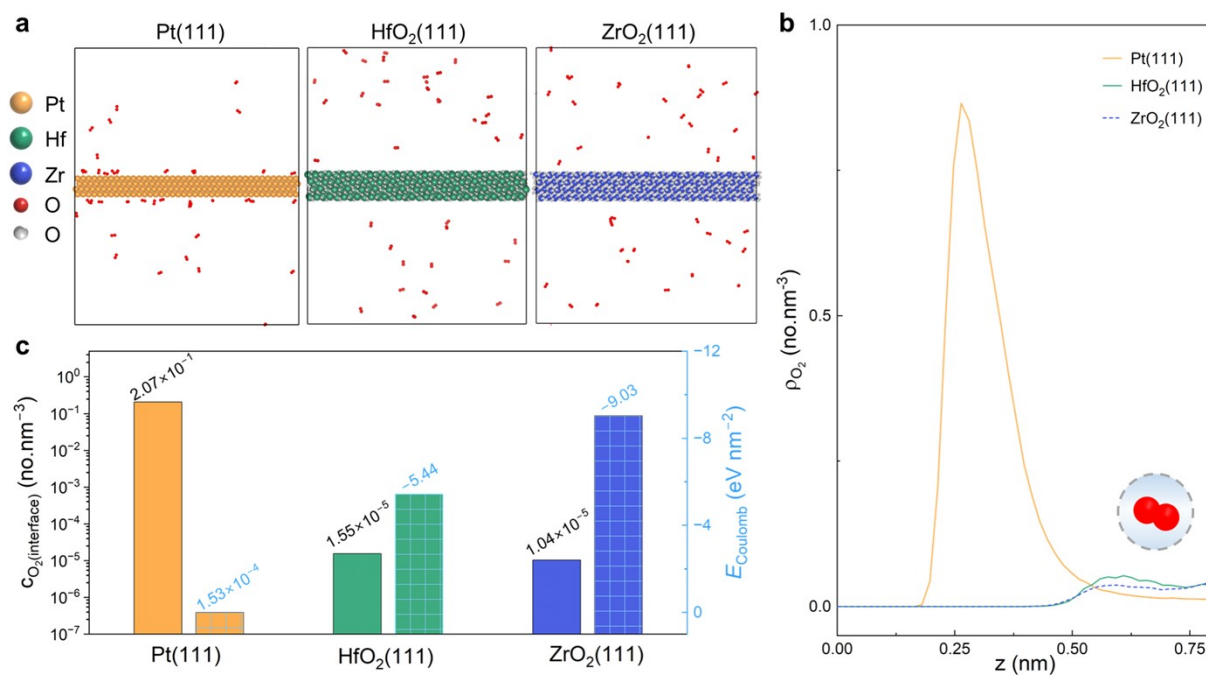
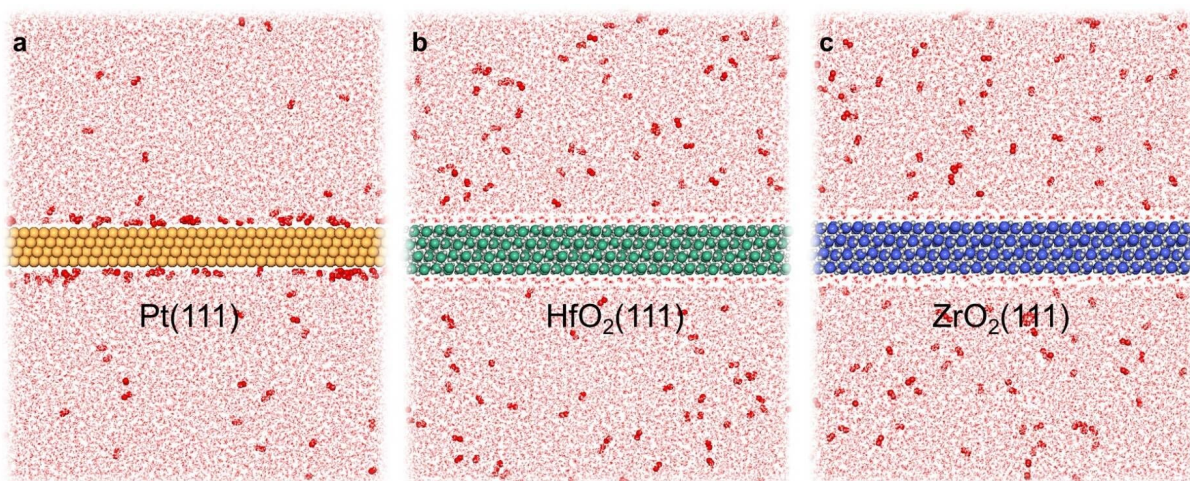**Fig. S10** Distributions of O_2 molecules at the catalyst/water interfaces. (a) Representative equilibrium simulation snapshots of studied multiphase models. The multiphase models consist of catalysts, O_2 molecules, and water. The catalysts from left to right are Pt(111), HfO_2(111), and ZrO_2(111). Orange, green, and blue balls represent Pt, Hf, and Zr atoms, respectively. The O atoms of O_2 molecules and the O atoms of HfO_2 and ZrO_2 are denoted by red and gray balls, respectively. H_2O molecules are not displayed to clearly show the distributions of O_2 molecules. (b) Number densities of O_2 molecules near catalyst surfaces. $z = 0$ represents the position of the catalytic site at the interface. (c) O_2(interface) concentrations and catalyst–water Coulomb interactions corresponding to the three systems. The O_2 concentration of the simulated system is about 50 times higher than the saturating concentration at atmospheric pressure and room temperature (298.15 K).
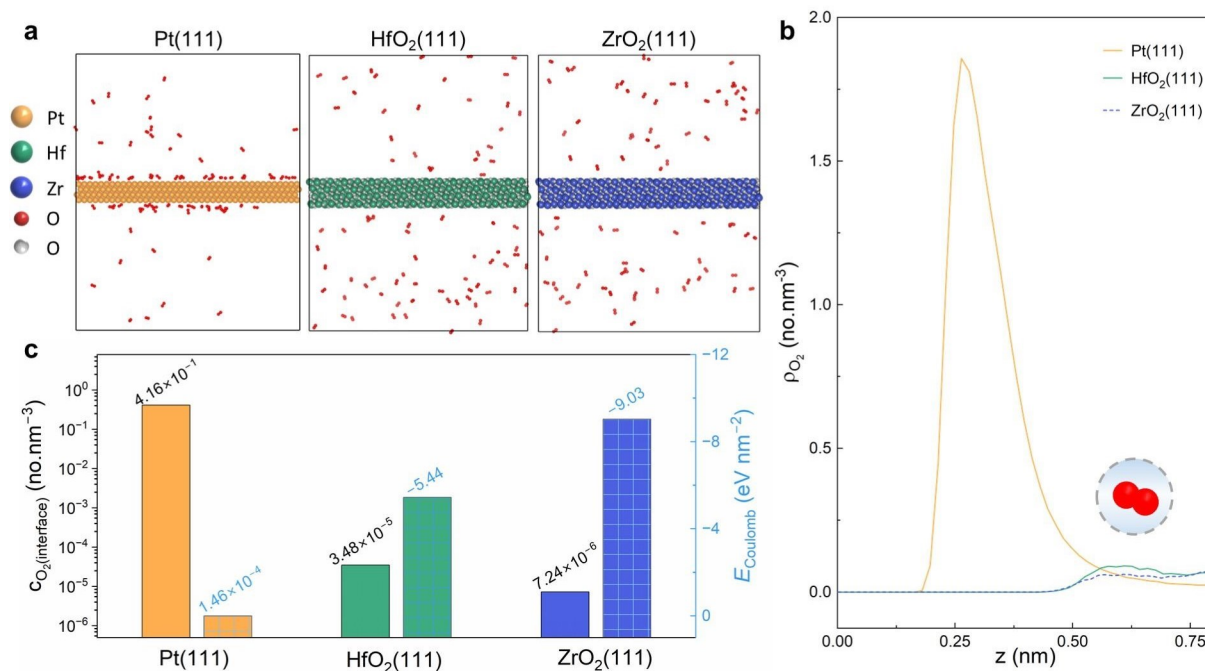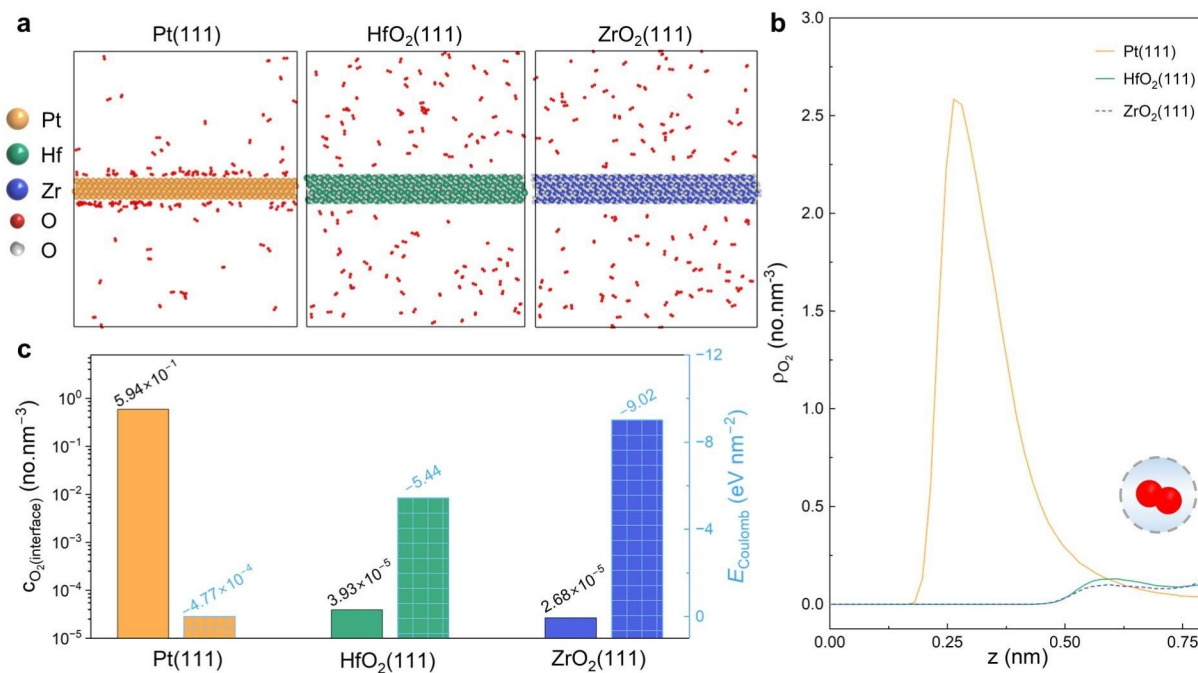
Fig. S11 Distributions of O_2 molecules at the catalyst/electrolyte interfaces. (a) Representative equilibrium simulation snapshots of studied multiphase models. The multiphase models consist of catalysts, O_2 molecules, and 0.1 M $HClO_4$ solution. The catalysts from left to right are Pt(111), HfO_2(111), and ZrO_2(111). Orange, green, and blue balls represent Pt, Hf, and Zr atoms, respectively. The O atoms of O_2 molecules and the O atoms of HfO_2 and ZrO_2 are denoted by red and gray balls, respectively. H_2O molecules, H_3O^+ ions, and ClO_4^- ions are not displayed to clearly show the distributions of O_2 molecules. (b) Number densities of O_2 molecules near catalyst surfaces. $z = 0$ represents the position of the catalytic site at the interface. (c) O_2(interface) concentrations and catalyst–water Coulomb interactions corresponding to the three systems.
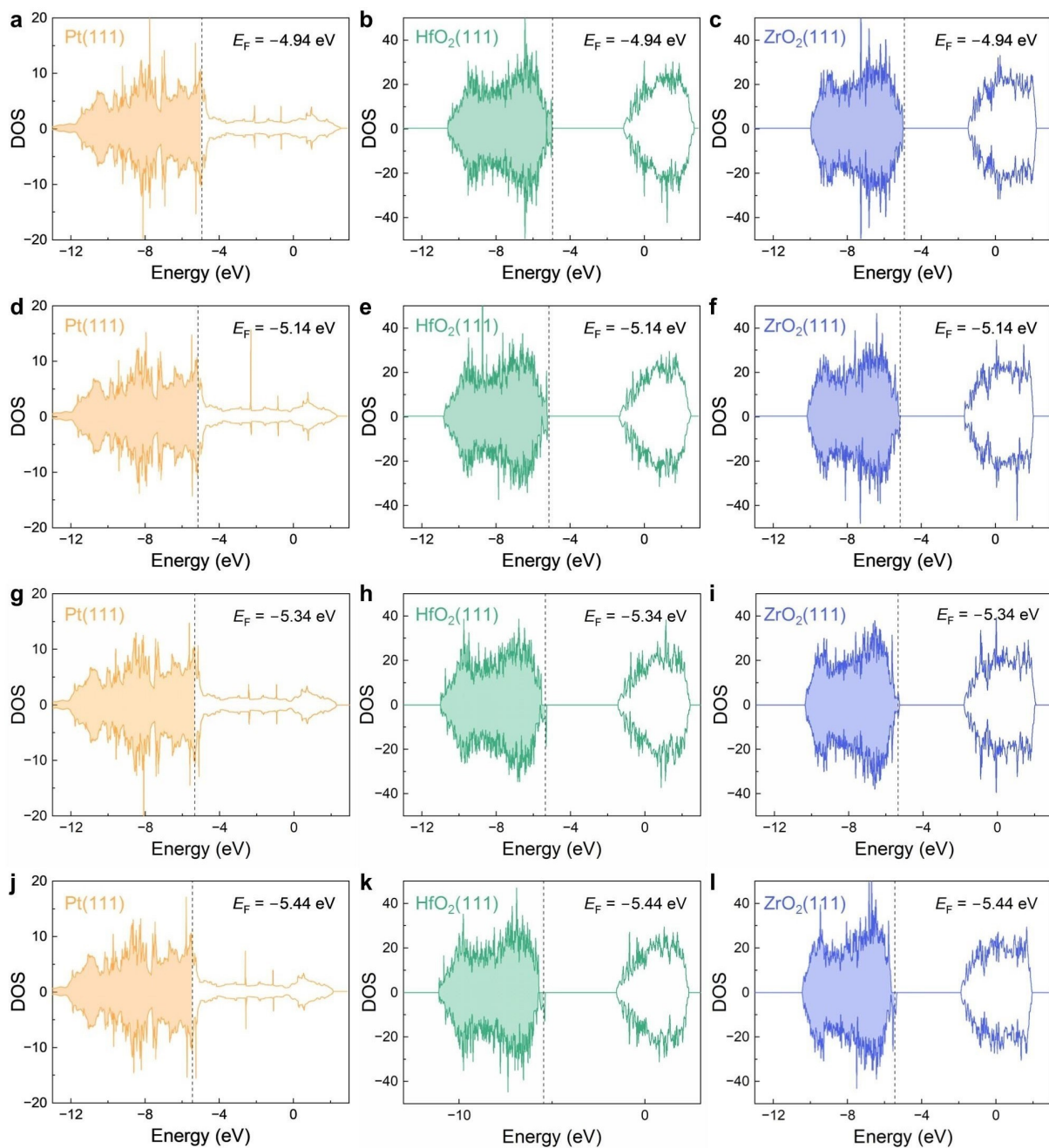
Fig. S12 Densities of states of Pt(111), HfO$_2$(111), and ZrO$_2$(111). (a)–(c) Densities of states of (a) Pt(111), (b) HfO$_2$(111), and (c) ZrO$_2$(111) at U = 0.4 V vs. RHE. (d)–(f) Densities of states of (d) Pt(111), (e) HfO$_2$(111), and (f) ZrO$_2$(111) at U = 0.6 V vs. RHE. (g)–(i) Densities of states of (g) Pt(111), (h) HfO$_2$(111), and (i) ZrO$_2$(111) at U = 0.8 V vs. RHE. (j)–(l) Densities of states of (j) Pt(111), (k) HfO$_2$(111), and (l) ZrO$_2$(111) at U = 0.9 V vs. RHE. The Fermi level is denoted by E_F and marked by a vertical dashed line.
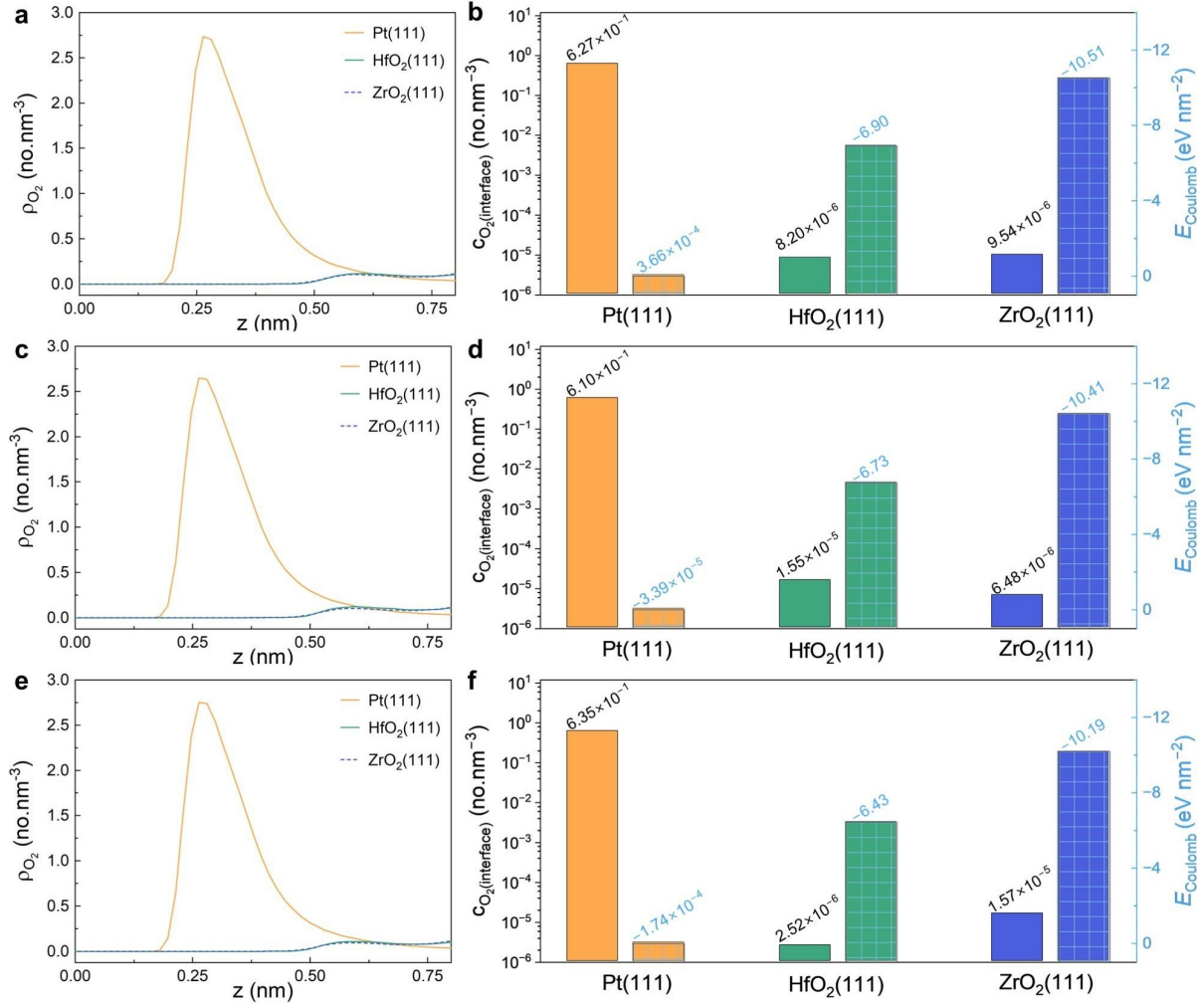
Fig. S13 Distributions of O_2 molecules at the catalyst/electrolyte interfaces in 0.1 M $HClO_4$ solution. (a) and (b) Results at $U = 0.4$ V vs. RHE. (c) and (d) Results at $U = 0.6$ V vs. RHE. (e) and (f) Results at $U = 0.8$ V vs. RHE. The involved catalysts are Pt(111), HfO_2(111), and ZrO_2(111). (a), (c) and (e) Number densities of O_2 molecules near catalyst surfaces. z = 0 represents the position of the catalytic site at the interface. (b), (d), and (f) O_2(interface) concentrations and catalyst–water Coulomb interactions corresponding to the three systems.
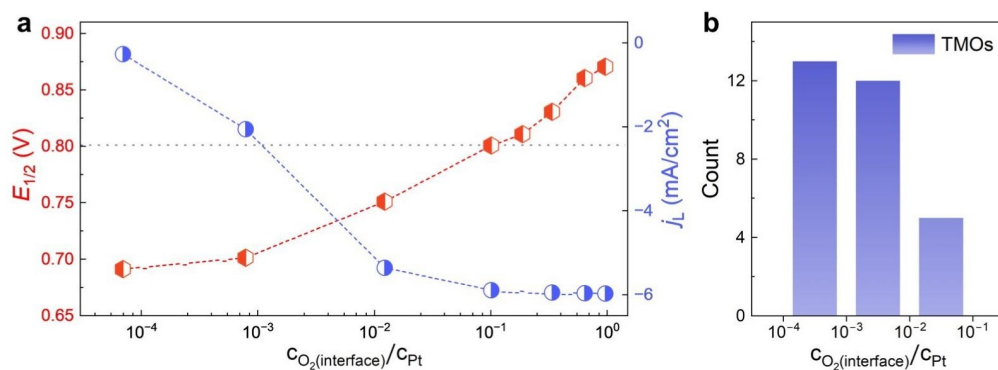
Fig. S14 (a) Half-wave potential ($E_{1/2}$) and diffusion-limiting current density (j_L) of Pt(111) as a function of the O_2(interface) concentration. c_{Pt} represents the O_2(interface) concentration of actual Pt(111). (b) Statistical distribution of the $c_{O_2(interface)}/c_{Pt}$ values of the 30 TMOs in Table S8.
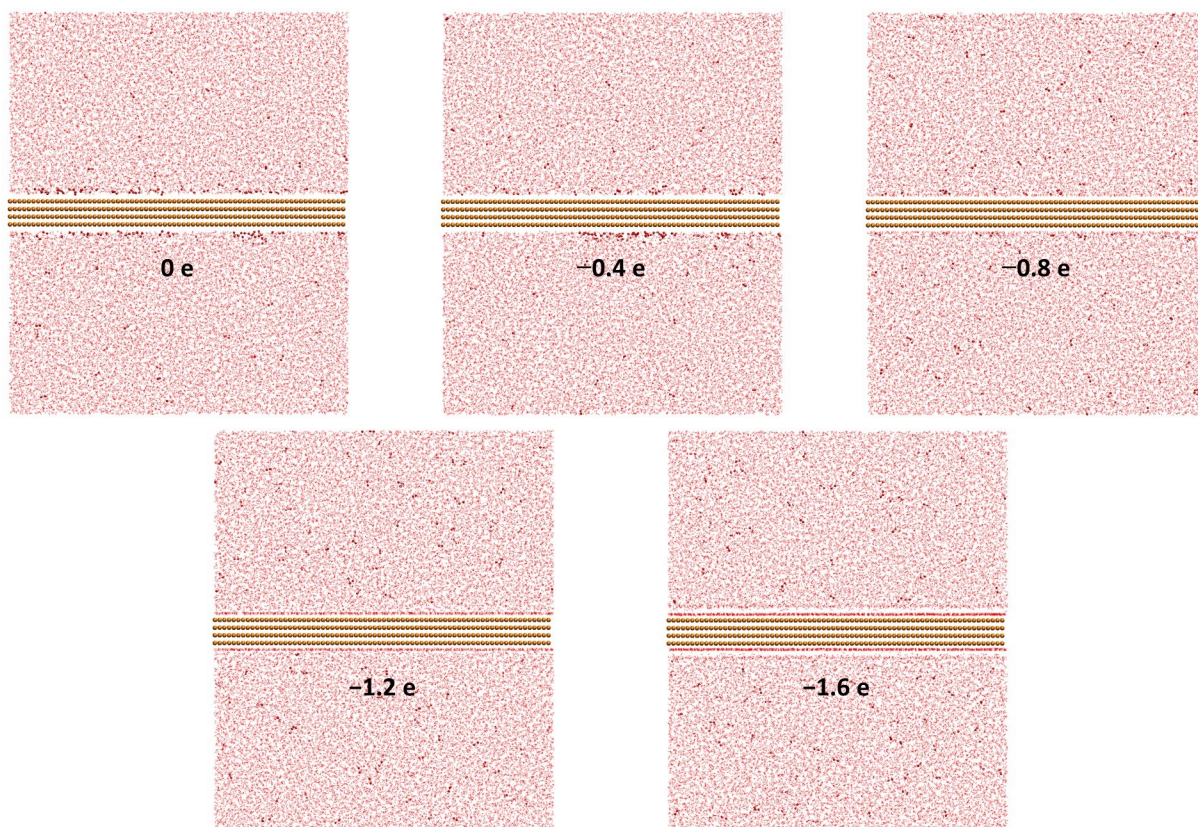
Fig. S15 Representative equilibrium simulation snapshots of the multiphase model consisting of Pt(111), O_2 molecules, and water at CCS = 0, −0.4, −0.8, −1.2, and −1.6 e. Orange and red balls represent Pt atoms and the O atoms of O_2 molecules, respectively. H_2O molecules are displayed in the line mode.
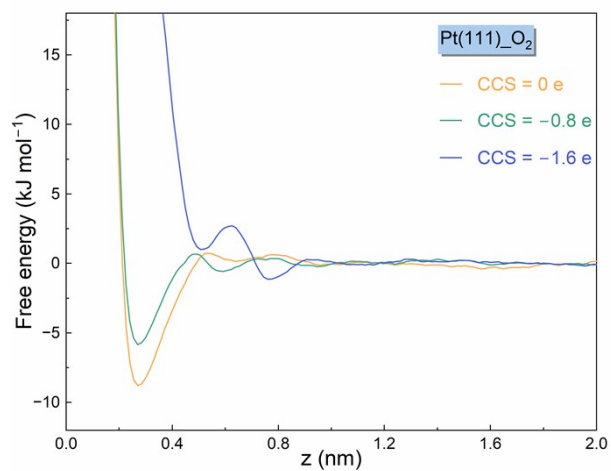
Fig. S16 Free energy profiles of O_2 movement towards Pt(111) in aqueous solution at CCS = 0, −0.8, and −1.6 e. z = 0 represents the position of the Pt site at the interface.
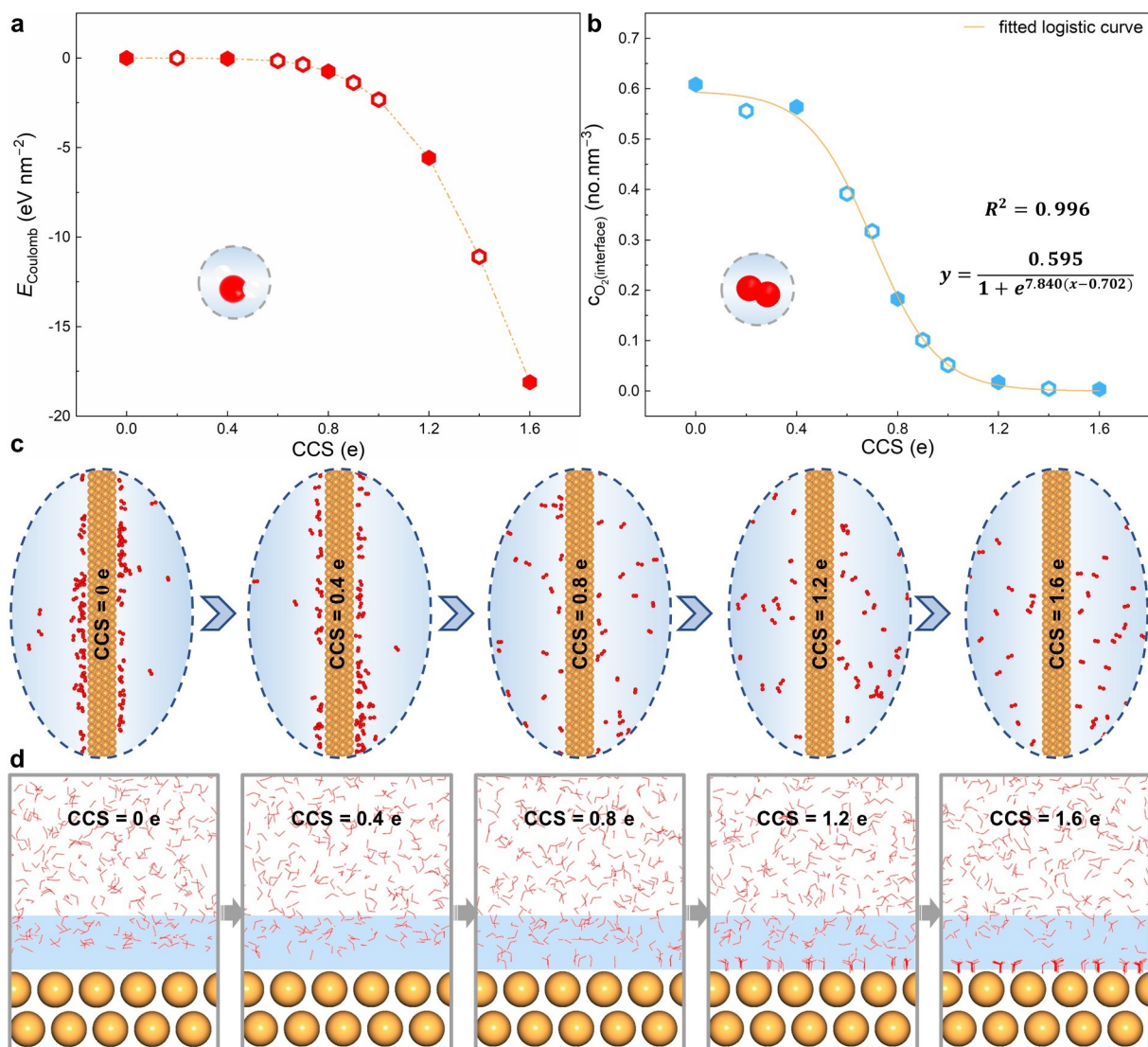
Fig. S17 Relation between the catalyst–water Coulomb interaction and the O_2(interface) concentration. (a) Catalyst–water Coulomb interaction as a function of CCS. (b) O_2(interface) concentration as a function of CCS. (c) and (d) Partial zones of representative equilibrium simulation snapshots at CCS = 0, 0.4, 0.8, 1.2, and 1.6 e. The whole snapshots are presented in Fig. S18. In (c), H_2O molecules are not displayed to clearly show the distribution of O_2 molecules. In contrast, in (d), O_2 molecules are hidden to clearly display the water wall at the interface. Red and orange balls denote the O atoms of O_2 molecules and Pt atoms, respectively. H_2O molecules are displayed in the line mode.
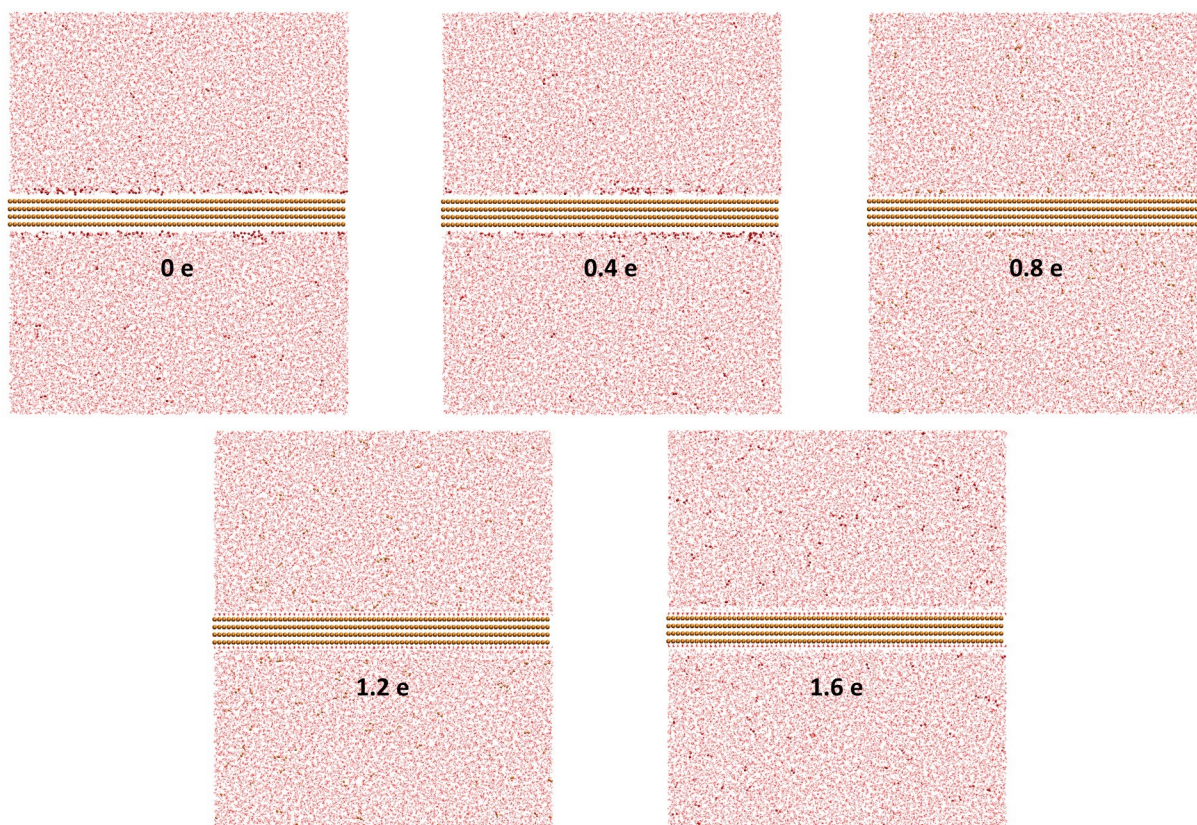
Fig. S18 Representative equilibrium simulation snapshots of the multiphase model consisting of Pt(111), O_2 molecules, and water at CCS = 0, 0.4, 0.8, 1.2, and 1.6 e. Orange and red balls represent Pt atoms and the O atoms of O_2 molecules, respectively. H_2O molecules are displayed in the line mode.
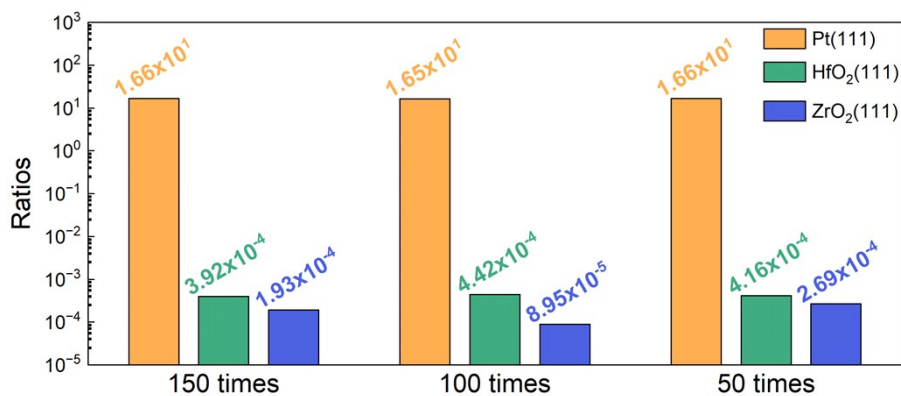
Fig. S19　Ratios of the O_2(interface) concentrations and the O_2 concentrations beyond the interfaces. The set O_2 concentrations in our simulation systems are about 150, 100, and 50 times higher than the real O_2 concentration, respectively. Although the set O_2 concentrations are different, the ratios remain almost unchanged. Therefore, it can be concluded that the ratio is not dependent on the set O_2 concentration.

a 1011169-FeO

Element	Charge (e)
Fe	1.005228
O	−1.005227

b 9017518-FeO$_3$

Element	Charge (e)
Fe	1.419261
O	−0.473085

c 1009013-Y$_2$O$_3$

Element	Charge (e)
Y	1.818818
O	−1.215204

d 1010093-NiO

Element	Charge (e)
Ni	1.025043
O	−1.025035

e 1010393-MnO

Element	Charge (e)
Mn	1.019042
O	−1.019047

f 1514112-Mn$_2$O$_7$

Element	Charge (e)
Mn	1.360424
O1	−0.561630
O2	−0.364037

g 1010278-La$_2$O$_3$

Element	Charge (e)
La	1.832782
O	−1.221867

Fig. S20 Partial charge distributions of TMOs: (a) FeO, (b) FeO$_3$, (c) Y$_2$O$_3$, (d) NiO, (e) MnO, (f) Mn$_2$O$_7$, and (g) La$_2$O$_3$. The numbers before the chemical formulae are the corresponding ID numbers in Crystal Open Database (http://www.crystallography.net/cod/).

a *Energy Environ. Sci.*, 2018, **11**, 2263

Cu-N-C (Cu-N$_2$)

Cu: 0.322076 e

Cu-N-C (Cu-N$_4$)

Cu: 0.556584 e

b *Energy Environ. Sci.*, 2018, **11**, 1980

Co@MCM

Co: 0.294534 e

c *Energy Environ. Sci.*, 2019, **12**, 2548

1.5Fe-ZIF

Fe: 0.467978 e

d *Energy Environ. Sci.*, 2019, **12**, 3508

Cu-SA/SNC

Cu: 0.416769 e

e *Energy Environ. Sci.*, 2021, **14**, 6455

Fe$_1$/d-CN

Fe: 0.538871 e

f *Energy Environ. Sci.*, 2019, **12**, 1317

f-FeCoNC900

Co: 0.093236 e

Fe: 0.352860 e

g *Energy Environ. Sci.*, 2022, **15**, 1601

Fe/Zn-N-C

Fe: 0.684201 e

Zn: 0.695345 e

h *Energy Environ. Sci.*, 2023, **16**, 2629

Fe-N,O/G

Fe: 0.441336 e

i *Energy Environ. Sci.*, 2023, **16**, 3576

Fe$_x$-N@CF

Fe1: 0.415508 e

Fe2: 0.415388 e

Fe$_x$/Cu-N@CF

Fe1: 0.518886 e

Fe2: 0.420302 e

Cu: 0.672142 e

j *Energy Environ. Sci.*, 2020, **13**, 3544

Fe/CoN-C

Fe: 0.533390 e

Co: 0.299023 e

k *Energy Environ. Sci.*, 2024, **17**, 123

As-DC1-1050

As: 0.028887 e

H C N O S Zn Fe Cu Co As

Fig. S21 Optimised structures and CCSs of SACs and DACs in Table S9. The structures are constructed by reference to those presented in their respective papers.

a *Energy Environ. Sci.*, 2018, **11**, 2348

FeN4/CNS

Fe: 0.549533 e

FeCl1N4/CNS

Fe: 0.538426 e

b *Energy Environ. Sci.*, 2022, **15**, 1183

4.2-FeSA

Fe1

Fe2

Fe1: 0.308787 e

Fe2: 0.308780 e

c *Energy Environ. Sci.*, 2024, **17**, 249

Fe-N$_4$P/NPC

Fe: 0.605273 e

Fe-N$_4$SP/NPS-HC

Fe: 0.508996 e

d *Energy Environ. Sci.*, 2024, **17**, 2298

ZnCoFe-TAC/NC

Zn: 0.719672 e

Co: 0.463595 e

Fe: 0.719060 e

ZnCoFe-TAC/SNC

Zn: 0.723261 e

Co: 0.462985 e

Fe: 0.413711 e

C   N   P   S   Cl   Zn   Fe   Co
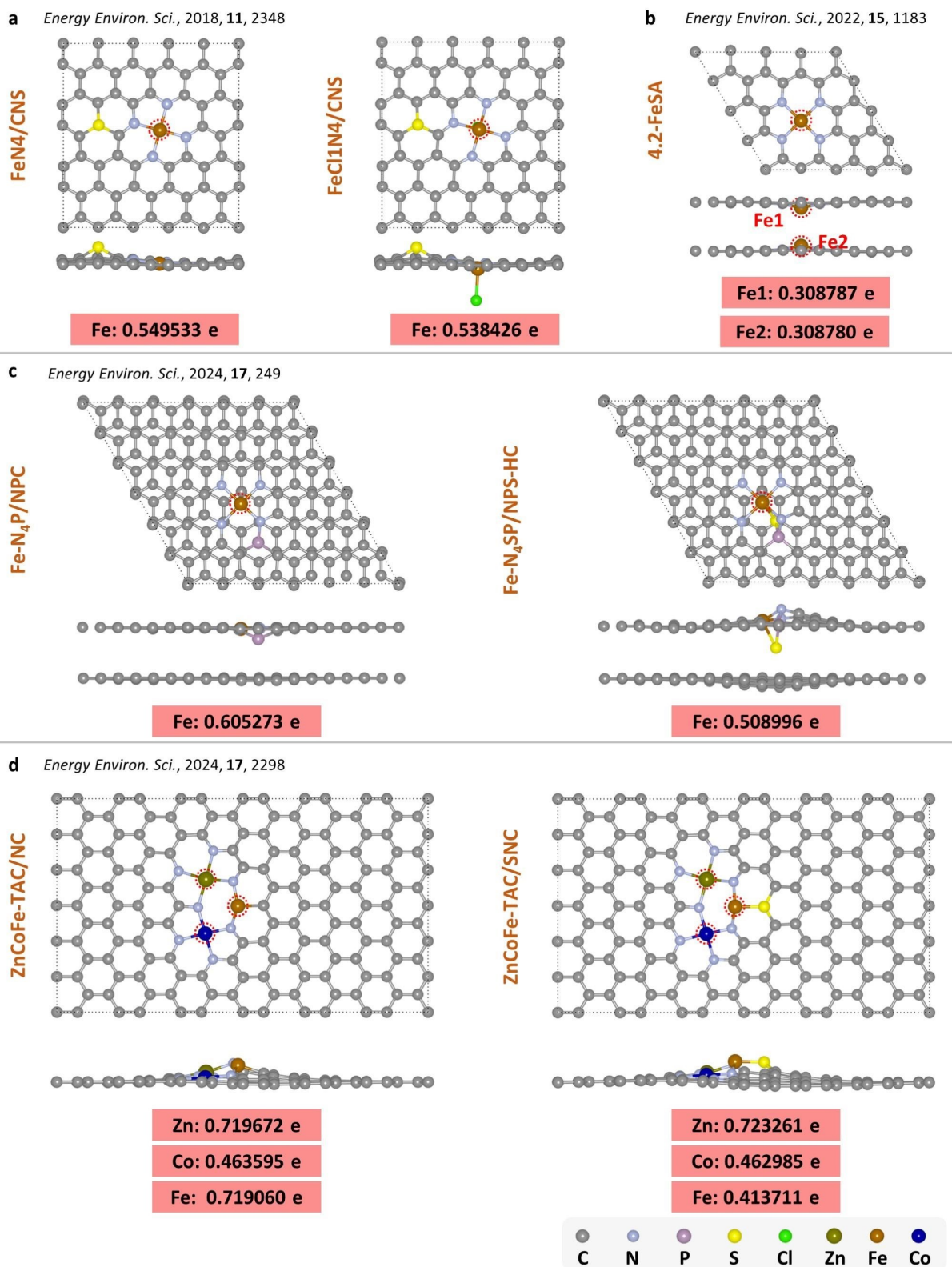
Fig. S22 Optimised structures and CCSs of SACs and DACs in Table S9. The structures are constructed by reference to those presented in their respective papers.
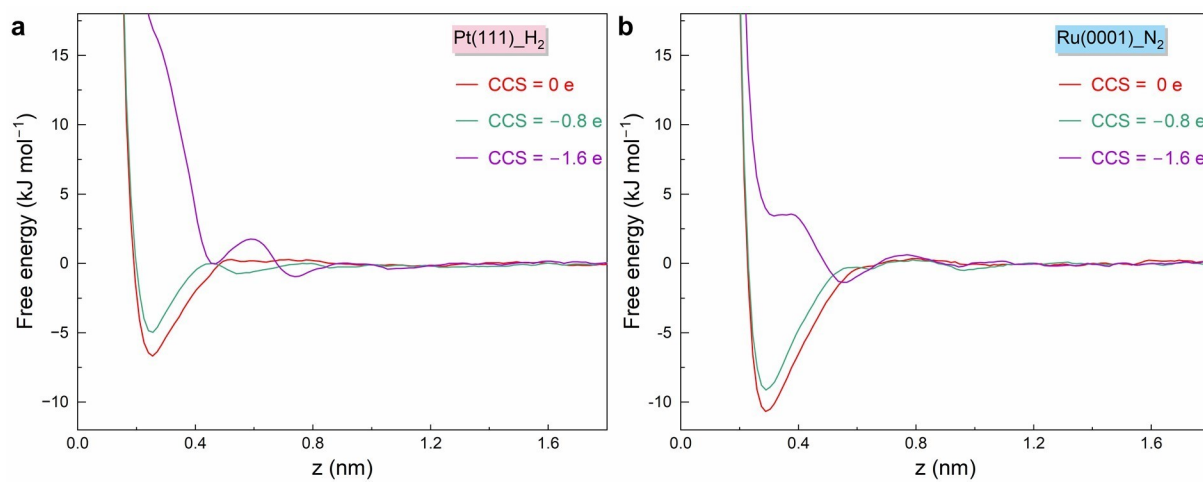
Fig. S23 Free energy profiles of (a) H_2 movement towards Pt(111) and (b) N_2 movement towards Ru(0001) in aqueous solution at CCS = 0, −0.8, and −1.6 e. z = 0 represents the position of the catalytic site at the interface.
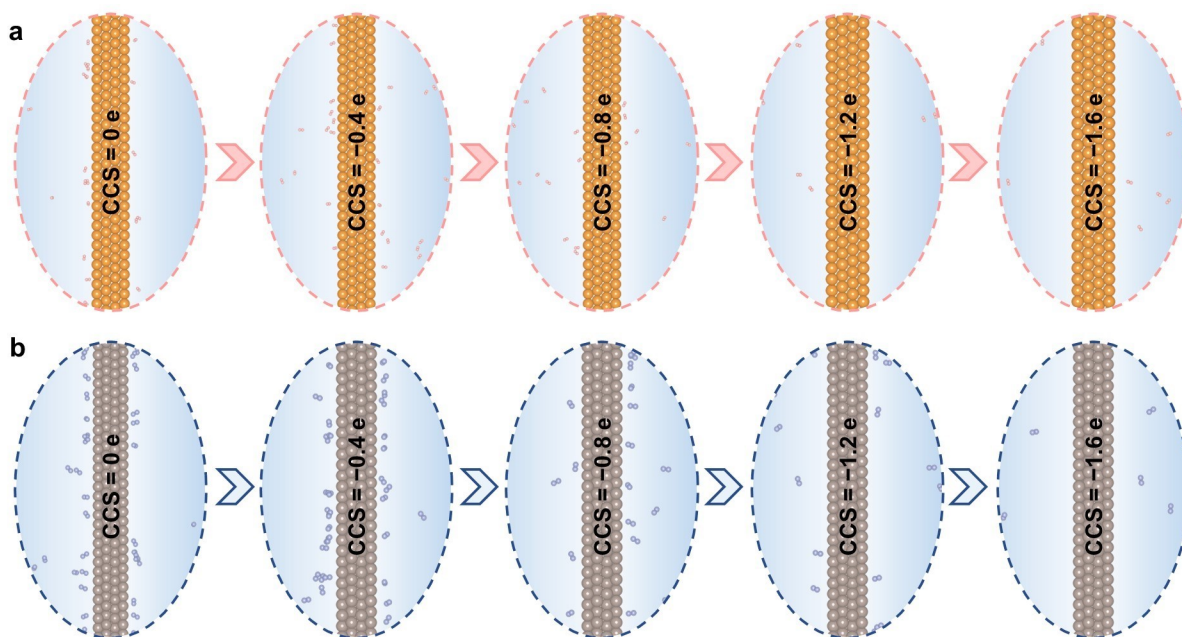
Fig. S24 Interfacial zones of the representative equilibrium simulation snapshots of studied multiphase models at CCS = 0, −0.4, −0.8, −1.2, and −1.6 e. (a) Snapshots for the multiphase model consisting of Pt(111), H_2 molecules, and water. (b) Snapshots for the multiphase model consisting of Ru(0001), N_2 molecules, and water. H_2O molecules are not displayed to clearly show the distribution of H_2 or N_2 molecules. Pink, orange, light blue, and greyish brown balls denote H, Pt, N, and Ru atoms, respectively.
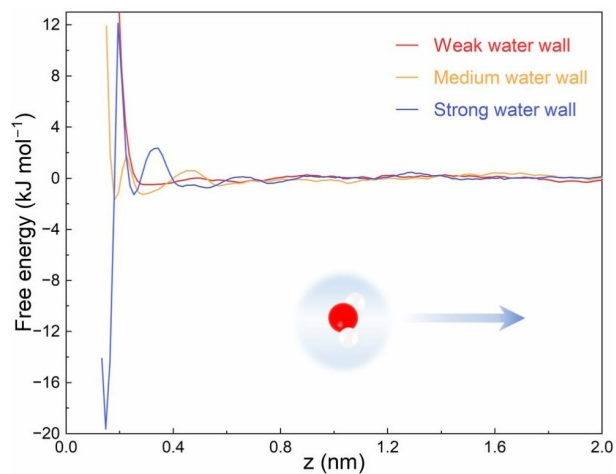
Fig. S25   Free energy profiles of the water dissociation from the Pt site in aqueous solution under the conditions of a weak water wall, a medium water wall, and a strong water wall. The three water walls correspond to the water walls of Pt(111) at CCS = 0, 0.8, and 1.6 e, respectively. z = 0 represents the position of the Pt site at the interface.
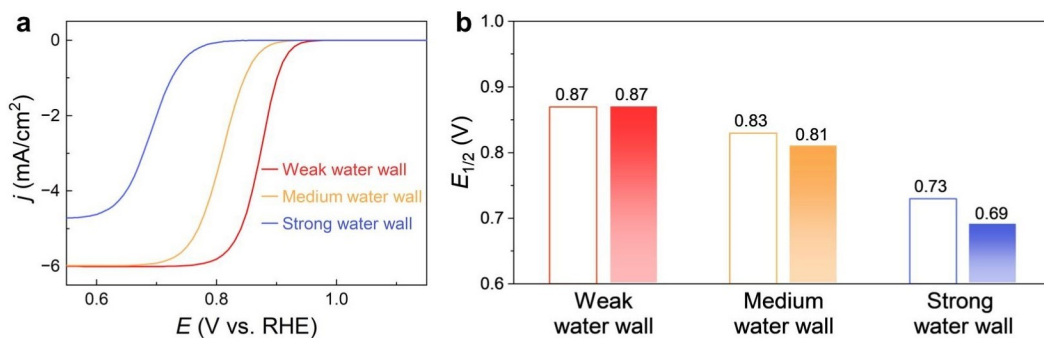
Fig. S26 (a) Polarization curves with the effect of the water dissociation under the conditions of a weak water wall, a medium water wall, and a strong water wall. The three water walls correspond to the water walls of Pt(111) at CCS = 0, 0.8, and 1.6 e, respectively. (b) Comparison of the half-wave potentials ($E_{1/2}$) in the absence (empty bar) and presence (shadowed bar) of water dissociation effect. The half-wave potentials in the absence of water dissociation effect were taken from Fig. 5.

Table S1 Geometric structure and partial charge distribution of the unit cell of the slab model of Pt(111). Lattice vectors are: [(2.804700, 0.000000, 0.000000), (0.000000, 4.857800, 0.000000), (0.000000, 0.000000, 36.869999)]. The unit is Angstrom (Å). An accuracy level of 0.03 falls within medium accuracy for the Gamma-centred k-point mesh. An accuracy level of 0.015 corresponds to the high level of accuracy. Comparing atomic charges calculated at medium and high k-point accuracy levels reveals that the differences between them are extremely small, which shows that an accuracy level of 0.03 is sufficient for achieving convergence.

Element	Cartesian coordinates (Å)			Charge (e)	
				Accuracy level: 0.03	Accuracy level: 0.015
Pt	0.000000	-0.025547	14.988798	−0.030475	−0.030354
Pt	1.402350	2.403353	14.988798	−0.030475	−0.030354
Pt	0.000000	1.619250	17.289817	0.030475	0.030354
Pt	1.402350	4.048150	17.289817	0.030474	0.030354
Pt	1.402350	0.809650	19.580182	0.030475	0.030354
Pt	0.000000	3.238550	19.580182	0.030475	0.030354
Pt	0.000000	0.025547	21.881201	−0.030475	−0.030354
Pt	1.402350	2.454447	21.881201	−0.030474	−0.030354

Table S2 Geometric structure and partial charge distribution of the unit cell of the slab model of HfO_2(111). Lattice vectors are: [(7.258087, 0.000000, 0.000000), (−2.917651, 5.944904, 0.000000), (0.000000, 0.000000, 41.970402)]. The unit is Angstrom (Å). An accuracy level of 0.03 falls within medium accuracy for the Gamma-centred k-point mesh. An accuracy level of 0.015 corresponds to the high level of accuracy. Comparing atomic charges calculated at medium and high k-point accuracy levels reveals that the differences between them are extremely small, which shows that an accuracy level of 0.03 is sufficient for achieving convergence.

Element	Cartesian coordinates (Å)			Charge (e)	
				Accuracy level: 0.03	Accuracy level: 0.015
Hf	0.244073	4.046863	16.114578	2.175749	2.175749
Hf	3.838342	5.819009	19.270878	2.187213	2.187213
Hf	3.166532	1.697205	22.508559	2.184041	2.184041
Hf	-0.420972	3.452931	25.556953	2.155163	2.155163
Hf	3.591809	3.737757	16.367408	2.115088	2.115088
Hf	-0.023736	5.581129	19.766381	2.174914	2.174914
Hf	6.522061	1.409489	22.932040	2.177177	2.177177
Hf	2.948926	3.171386	26.144916	2.166810	2.166811
Hf	1.080885	0.705095	16.413281	2.155262	2.155262
Hf	4.751830	2.460631	19.461843	2.183617	2.183618
Hf	1.162220	4.283618	22.699272	2.187372	2.187372
Hf	0.415689	0.110878	25.855992	2.175107	2.175107
Hf	4.968813	0.986801	15.825528	2.166362	2.166362
Hf	1.396207	2.748020	19.038362	2.178588	2.178588
Hf	-2.233610	4.521623	22.203854	2.175869	2.175869
Hf	4.326007	0.420346	25.603372	2.113944	2.113944
O	-0.297548	1.973619	15.476166	−1.093061	−1.093061
O	3.255307	3.863349	18.722325	−1.102430	−1.102431
O	-0.372649	5.677912	21.913418	−1.115553	−1.115553
O	6.172885	1.517633	25.057967	−1.127672	−1.127672
O	2.056348	4.754871	15.357306	−1.065284	−1.065284
O	1.437594	0.575657	18.483807	−1.096001	−1.096001
O	5.082022	2.383211	21.687576	−1.106215	−1.106215
O	1.431161	4.188542	24.845764	−1.140467	−1.140468
O	1.744798	2.640209	16.912645	−1.128391	−1.128391
O	-1.885055	4.424667	20.056942	−1.115350	−1.115350
O	4.662787	0.294439	23.247448	−1.102069	−1.102069
O	0.957315	2.184645	26.494194	−1.093061	−1.093061
O	3.569546	5.914383	17.124638	−1.141309	−1.141309
O	2.836407	1.774590	20.282700	−1.106861	−1.106861
O	-0.776992	3.581912	23.486595	−1.096553	−1.096553

O	2.943796	5.348077	26.613516	−1.065231	−1.065231
O	2.998335	0.215479	15.888567	−1.081421	−1.081421
O	-0.519391	2.007071	19.212077	−1.075966	−1.075966
O	3.126599	3.812729	22.413915	−1.065210	−1.065210
O	-0.474519	5.541209	25.915758	−1.088217	−1.088217
O	4.559958	2.106048	17.440633	−1.063886	−1.063886
O	0.953951	3.947523	20.634286	−1.067990	−1.067990
O	-2.599591	5.721821	23.870079	−1.061393	−1.061393
O	3.817912	1.656381	27.051267	−0.984308	−0.984308
O	-1.783404	4.561697	16.054854	−1.088427	−1.088427
O	4.791599	0.344953	19.556277	−1.065016	−1.065016
O	1.179821	2.150212	22.758115	−1.076047	−1.076047
O	4.919701	3.942577	26.082129	−1.081655	−1.081655
O	4.099481	2.501699	14.919177	−0.984556	−0.984556
O	0.341865	4.380669	18.100491	−1.061283	−1.061283
O	6.964023	0.210081	21.335906	−1.067437	−1.067437
O	3.357800	2.051569	24.529979	−1.063957	−1.063957

Table S3 Geometric structure and partial charge distribution of the unit cell of the slab model of $ZrO_2(111)$. Lattice vectors are: [(7.334865, 0.000000, 0.000000), (−2.942679, 6.003801, 0.000000), (0.000000, 0.000000, 42.086899)]. The unit is Angstrom (Å). An accuracy level of 0.03 falls within medium accuracy for the Gamma-centred k-point mesh. An accuracy level of 0.015 corresponds to the high level of accuracy. Comparing atomic charges calculated at medium and high k-point accuracy levels reveals that the differences between them are extremely small, which shows that an accuracy level of 0.03 is sufficient for achieving convergence.

Element	Cartesian coordinates (Å)			Charge (e)	
				Accuracy level: 0.03	Accuracy level: 0.015
Zr	1.957931	0.759937	16.39142	2.331007	2.331293
Zr	5.650153	2.623619	19.80913	2.408330	2.408472
Zr	1.991934	4.419428	23.00685	2.411083	2.411186
Zr	1.331231	0.19256	26.25246	2.371020	2.371130
Zr	3.806204	3.697237	16.4168	2.356269	2.356381
Zr	0.190554	5.473431	19.50185	2.416701	2.416844
Zr	-0.48776	1.316219	22.77251	2.421997	2.421610
Zr	3.155756	3.107946	25.95962	2.383737	2.383509
Zr	5.907516	1.05844	16.12745	2.383644	2.383410
Zr	2.216271	2.849752	19.31431	2.420410	2.420463
Zr	-1.40446	4.696119	22.58501	2.417409	2.417438
Zr	5.257273	0.469059	25.67002	2.357324	2.357581
Zr	0.397396	3.974138	15.83419	2.371656	2.371528
Zr	4.12901	5.750327	19.0801	2.411256	2.411439
Zr	3.413062	1.542238	22.27782	2.408759	2.408395
Zr	-0.22951	3.406473	25.69582	2.330916	2.331180
O	-0.46664	5.512444	14.93445	−1.038060	−1.038012
O	6.010886	1.408035	18.12969	−1.172897	−1.173002
O	2.431616	3.202175	21.40174	−1.177109	−1.176984
O	-1.19905	5.07996	24.62138	−1.174389	−1.174635
O	-1.59901	3.197769	15.87762	−1.180102	−1.180072
O	2.19156	5.013012	19.24954	−1.182589	−1.182601
O	1.493834	0.837692	22.47908	−1.171594	−1.171272
O	5.198736	2.591114	26.0063	−1.202490	−1.202453
O	4.477678	5.646071	16.93884	−1.242345	−1.242404
O	3.759776	1.447624	20.1127	−1.239100	−1.239260
O	0.100068	3.284812	23.33946	−1.224131	−1.223991
O	3.697054	5.197953	26.60923	−1.211828	−1.211714
O	1.942634	2.950262	17.1388	−1.256102	−1.256238
O	-1.73706	4.779728	20.32667	−1.230875	−1.230970

O	4.898792	0.602391	23.56403	−1.221069	−1.221166
O	1.328479	2.392413	26.71495	−1.175914	−1.175847
O	0.400014	1.774231	15.37266	−1.176229	−1.176102
O	4.164781	3.563934	18.52287	−1.220794	−1.220933
O	0.523062	5.389948	21.76023	−1.231499	−1.231285
O	-0.21408	1.216268	24.94823	−1.255852	−1.255907
O	2.423543	4.97218	15.47737	−1.211599	−1.211485
O	1.628669	0.881034	18.74727	−1.224172	−1.224183
O	5.30366	2.718245	21.97433	−1.239812	−1.239775
O	1.642762	4.523828	25.1481	−1.242566	−1.242712
O	3.864337	1.575271	16.08098	−1.202158	−1.202197
O	0.234455	3.327631	19.60715	−1.170722	−1.170812
O	3.929247	5.156737	22.83804	−1.182723	−1.182833
O	3.327459	0.968179	26.20848	−1.180758	−1.180780
O	-0.01494	5.089602	17.46535	−1.174144	−1.174328
O	6.631469	0.963424	20.68495	−1.177608	−1.177592
O	3.051981	2.757378	23.95742	−1.172617	−1.172586
O	-0.74788	4.658061	27.15241	−1.037671	−1.037727

Table S4 Catalyst–water Coulomb interactions of Ni(111), Cu(111), Pt(111), Ag(111), Au(111), RuO_2(110), IrO_2(110), HfO_2(111), ZrO_2(111), and MnO_2(110).

Materials		$E_{Coulomb}$ (eV nm^{-2})
Transitional metal	Ni(111)	-9.40×10^{-6}
	Cu(111)	7.39×10^{-6}
Noble metal	Pt(111)	1.34×10^{-4}
	Ag(111)	1.37×10^{-4}
	Au(111)	8.11×10^{-4}
Noble metal oxides	RuO_2(110)	-2.36
	IrO_2(110)	-1.85
Transitional metal oxides	HfO_2(111)	-5.44
	ZrO_2(111)	-9.03
	MnO_2(110)	-2.15

Table S5 Atomic charges of the unit cell of the Pt(111) slab model at $U = 0.4$ V, 0.6 V, 0.8 V and 0.9 V vs. RHE.

Atom	Charge (e)			
	Low potential		High potential	
	0.4 V	0.6 V	0.8 V	0.9 V
Pt1	−0.069797	−0.054301	−0.038525	−0.030882
Pt2	−0.069799	−0.054301	−0.038525	−0.030881
Pt3	0.033548	0.032301	0.031025	0.030381
Pt4	0.033548	0.032301	0.031025	0.030381
Pt5	0.033548	0.032301	0.031025	0.030382
Pt6	0.033548	0.032301	0.031025	0.030382
Pt7	−0.069797	−0.054301	−0.038525	−0.030882
Pt8	−0.069799	−0.054301	−0.038525	−0.030881

Table S6 Atomic charges of the unit cell of the HfO$_2$(111) slab model at U = 0.4 V, 0.6 V, 0.8 V and 0.9 V vs. RHE.

Atom	Charge (e)			
	Low potential		High potential	
	0.4 V	0.6 V	0.8 V	0.9 V
Hf1	2.272556	2.282281	2.306162	2.315994
Hf2	2.188521	2.188861	2.192065	2.193804
Hf3	2.183970	2.184700	2.187072	2.187198
Hf4	2.291917	2.307878	2.341384	2.355257
Hf5	2.120265	2.122065	2.124935	2.125601
Hf6	2.178834	2.180145	2.182498	2.184121
Hf7	2.178652	2.180369	2.182635	2.183282
Hf8	2.291307	2.301010	2.324133	2.335186
Hf9	2.291932	2.307667	2.341035	2.354886
Hf10	2.183591	2.184204	2.185977	2.186833
Hf11	2.187436	2.188684	2.192578	2.193416
Hf12	2.272251	2.282494	2.305975	2.315638
Hf13	2.290998	2.300459	2.324500	2.335643
Hf14	2.179224	2.179509	2.182429	2.182948
Hf15	2.178788	2.179770	2.182954	2.183756
Hf16	2.120288	2.122916	2.124985	2.126128
O1	−1.130387	−1.126113	−1.117088	−1.113451
O2	−1.101150	−1.100251	−1.099064	−1.098455
O3	−1.114685	−1.113910	−1.113984	−1.113651
O4	−1.156461	−1.158364	−1.161877	−1.162556
O5	−1.109055	−1.105281	−1.097900	−1.094873
O6	−1.116751	−1.118569	−1.122886	−1.124889
O7	−1.107100	−1.106801	−1.106281	−1.105820
O8	−1.164825	−1.167452	−1.171910	−1.173904
O9	−1.156178	−1.158031	−1.161937	−1.163221
O10	−1.115099	−1.114519	−1.113873	−1.113901
O11	−1.100660	−1.100954	−1.099243	−1.098280
O12	−1.130020	−1.126594	−1.117084	−1.113403
O13	−1.164685	−1.167046	−1.171790	−1.173534
O14	−1.106855	−1.106339	−1.105750	−1.105474
O15	−1.116326	−1.118627	−1.123329	−1.124865
O16	−1.109003	−1.105760	−1.097719	−1.094844
O17	−1.120279	−1.115745	−1.105013	−1.100714
O18	−1.075243	−1.074038	−1.071865	−1.070786

O19	−1.064341	−1.064263	−1.063688	−1.063157
O20	−1.111159	−1.106526	−1.094957	−1.090264
O21	−1.080743	−1.083185	−1.089828	−1.092718
O22	−1.066925	−1.065864	−1.064774	−1.064101
O23	−1.081018	−1.082760	−1.087591	−1.089259
O24	−1.105818	−1.081397	−1.023205	−0.997323
O25	−1.111477	−1.106320	−1.094528	−1.089827
O26	−1.064925	−1.064441	−1.063442	−1.063236
O27	−1.075632	−1.074044	−1.071992	−1.070657
O28	−1.120139	−1.115856	−1.105117	−1.100744
O29	−1.105415	−1.081302	−1.022629	−0.997039
O30	−1.080741	−1.082818	−1.087498	−1.089015
O31	−1.066529	−1.065867	−1.064193	−1.063600
O32	−1.080904	−1.083972	−1.089284	−1.092129

Table S7 Atomic charges of the unit cell of the ZrO$_2$(111) slab model at U = 0.4 V, 0.6 V, 0.8 V and 0.9 V vs. RHE.

Atom	Charge (e)			
	Low potential		High potential	
	0.4 V	0.6 V	0.8	0.9 V
Zr1	2.336551	2.338605	2.344611	2.347174
Zr2	2.411051	2.412637	2.416164	2.418454
Zr3	2.412003	2.412670	2.415423	2.416212
Zr4	2.503092	2.510930	2.530539	2.541068
Zr5	2.502037	2.514362	2.540382	2.553501
Zr6	2.415651	2.416322	2.418458	2.419479
Zr7	2.420320	2.421287	2.424115	2.425688
Zr8	2.480272	2.488164	2.506830	2.516778
Zr9	2.480197	2.487194	2.507210	2.516564
Zr10	2.419514	2.420984	2.424738	2.426653
Zr11	2.416439	2.417036	2.419443	2.420366
Zr12	2.501714	2.514500	2.541058	2.554112
Zr13	2.502622	2.510801	2.530680	2.540377
Zr14	2.411998	2.413031	2.414548	2.416396
Zr15	2.411628	2.413357	2.417473	2.420111
Zr16	2.337621	2.338995	2.344430	2.347614
O1	−1.164794	−1.143613	−1.089588	−1.060768
O2	−1.192880	−1.194671	−1.199093	−1.200637
O3	−1.175204	−1.174687	−1.173453	−1.172368
O4	−1.192813	−1.194293	−1.200300	−1.203225
O5	−1.222474	−1.216179	−1.202258	−1.195967
O6	−1.181762	−1.180625	−1.177758	−1.176710
O7	−1.170065	−1.169542	−1.169491	−1.169228
O8	−1.224050	−1.217361	−1.203016	−1.196797
O9	−1.273210	−1.274451	−1.276715	−1.277928
O10	−1.238692	−1.238598	−1.238676	−1.238645
O11	−1.222896	−1.222410	−1.221338	−1.221197
O12	−1.247241	−1.241143	−1.227751	−1.221208
O13	−1.282784	−1.284387	−1.287772	−1.288404
O14	−1.231704	−1.231138	−1.230073	−1.230216
O15	−1.243200	−1.244522	−1.248608	−1.250283
O16	−1.217791	−1.213092	−1.203118	−1.198924
O17	−1.217414	−1.212847	−1.202922	−1.198624
O18	−1.242534	−1.244722	−1.248100	−1.250226

O19	−1.232005	−1.231685	−1.231217	−1.231473
O20	−1.282315	−1.283919	−1.287113	−1.288693
O21	−1.247049	−1.240931	−1.227690	−1.221198
O22	−1.222660	−1.221674	−1.221478	−1.221477
O23	−1.239400	−1.239369	−1.239059	−1.238878
O24	−1.273066	−1.274744	−1.276993	−1.278138
O25	−1.223986	−1.216828	−1.202887	−1.196555
O26	−1.169647	−1.169343	−1.168863	−1.168530
O27	−1.181683	−1.180330	−1.177948	−1.176187
O28	−1.222487	−1.216099	−1.202217	−1.196597
O29	−1.192572	−1.194515	−1.200063	−1.202582
O30	−1.175642	−1.174565	−1.172630	−1.172554
O31	−1.193588	−1.195283	−1.198889	−1.200636
O32	−1.165051	−1.143309	−1.089025	−1.060698

Table S8 O_2(interface) concentrations and catalyst–water Coulomb interactions of Pt(111) and all 30 TMO models provided by Nørskov et al., which are available at https://github.com/cattheory-oxides/data/tree/main/Transition%20metal%20oxide_adsorption_coordinates. c_{Pt} represents the O_2(interface) concentration of actual Pt(111) (*i.e.*, 5.87×10^{-1}). $c_{O_2(interface)}$ without $E_{Coulomb}$ represents the O_2(interface) concentration without considering the catalyst–water Coulomb interaction in the simulation. Notably, the sensitivity of the O_2(interface) concentration to the catalyst–water Coulomb interaction varies among different TMOs. For example, while $CoSb_2O_6\_101$ and $FeSb_2O_6\_212$ have almost the same catalyst–water Coulomb interactions, there is an apparent difference in their O_2(interface) concentrations. The variation should be due to differences in surface structure and chemical composition. However, the variation does not undermine the conclusion that the low O_2(interface) concentrations of TMOs are due to their strong catalyst–water Coulomb interactions, because the O_2(interface) concentrations of all 30 TMOs markedly increase when not considering the catalyst–water Coulomb interactions in the simulations.

Materials	$c_{O_2(interface)}$ (no.nm^{-3})	$c_{O_2(interface)}/c_{Pt}$	$E_{Coulomb}$ (eV nm^{-2})	$c_{O_2(interface)}$ (no.nm^{-3}) (without $E_{Coulomb}$)
Pt(111)	5.87×10^{-1}	1	1.34×10^{-4}	6.08×10^{-1}
$CoSb_2O_6\_100$	5.43×10^{-4}	9.25×10^{-4}	-3.73	2.29×10^{-1}
$CoSb_2O_6\_101$	3.96×10^{-4}	6.74×10^{-4}	-3.47	4.59×10^{-1}
$CoSb_2O_6\_110$	6.23×10^{-4}	1.06×10^{-3}	-2.46	1.75×10^{-1}
$CoSb_2O_6\_111$	1.31×10^{-3}	2.24×10^{-3}	-2.79	2.03×10^{-1}
$CoSb_2O_6\_112$	1.01×10^{-3}	1.72×10^{-3}	-2.47	4.42×10^{-1}
$Fe_2Mo_3O_{12}\_101$	1.83×10^{-2}	3.12×10^{-2}	-2.29	2.61×10^{-1}
$Fe_2Mo_3O_{12}\_110$	3.20×10^{-2}	5.45×10^{-2}	-1.93	2.33×10^{-1}
$Fe_2Mo_3O_{12}\_111$	4.08×10^{-2}	6.95×10^{-2}	-2.11	1.47×10^{-1}
$Fe_2Mo_3O_{12}\_2\_010$	3.37×10^{-2}	5.74×10^{-2}	-2.02	3.40×10^{-1}
$Fe_2Mo_3O_{12}\_2\_100$	1.92×10^{-2}	3.27×10^{-2}	-2.88	5.26×10^{-1}
$FeSb_2O_6\_100$	8.18×10^{-4}	1.39×10^{-3}	-3.80	2.99×10^{-1}
$FeSb2O_6\_111$	4.09×10^{-4}	6.97×10^{-4}	-3.54	2.20×10^{-1}
$FeSb_2O_6\_112$	6.11×10^{-4}	1.04×10^{-3}	-4.04	4.36×10^{-1}
$FeSb_2O_6\_212$	3.84×10^{-3}	6.55×10^{-3}	-3.45	2.89×10^{-1}
$FeSbO_4\_100$	1.70×10^{-4}	2.90×10^{-4}	-3.52	2.10×10^{-1}
$FeSbO_4\_112$	1.12×10^{-3}	1.91×10^{-3}	-5.64	2.86×10^{-1}
$FeSbO_4\_201$	1.49×10^{-4}	2.54×10^{-4}	-4.13	1.63×10^{-1}
$FeSbO_4\_211$	2.14×10^{-4}	3.65×10^{-4}	-4.99	2.04×10^{-1}
$FeSbO_4\_2\_111$	4.79×10^{-4}	8.16×10^{-4}	-5.18	2.02×10^{-1}
$FeSbO_4\_2\_211$	3.00×10^{-4}	5.11×10^{-4}	-5.16	2.03×10^{-1}
$FeSbO_4\_2\_221$	2.54×10^{-4}	4.33×10^{-4}	-4.76	2.52×10^{-1}
$FeSbO_4\_3\_100$	3.41×10^{-4}	5.81×10^{-4}	-3.81	2.34×10^{-1}

FeSbO$_4$_3_110	4.74×10^{-4}	8.07×10^{-4}	−4.48	2.00×10^{-1}
FeSbO$_4$_3_111	6.65×10^{-4}	1.13×10^{-3}	−4.71	1.83×10^{-1}
FeSbO$_4$_3_112	6.81×10^{-5}	1.16×10^{-4}	−4.13	2.20×10^{-1}
FeSbO$_4$_3_210	1.71×10^{-3}	2.91×10^{-3}	−4.02	1.37×10^{-1}
FeSbO$_4$_3_211	1.41×10^{-3}	2.40×10^{-3}	−4.11	2.93×10^{-1}
NiSb$_2$O$_6$_101	1.02×10^{-3}	1.73×10^{-3}	−2.53	3.69×10^{-1}
NiSb$_2$O$_6$_211	2.34×10^{-3}	3.99×10^{-3}	−2.92	2.44×10^{-1}
NiSb$_2$O$_6$-Ir	4.33×10^{-4}	7.37×10^{-4}	−3.45	2.24×10^{-1}

Table S9   Summary of experimentally reported SACs and DACs (published in *Energy & Environmental Science*) with a half-wave potential of greater than or equal to 0.85 V.

Catalysts	Reference
Co@MCM	*Energy Environ. Sci.*, 2018, **11**, 1980
Cu-N-C	*Energy Environ. Sci.*, 2018, **11**, 2263
FeN4/CNS FeCl1N4/CNS	*Energy Environ. Sci.*, 2018, **11**, 2348
f-FeCoNC900	*Energy Environ. Sci.*, 2019, **12**, 1317
1.5Fe-ZIF	*Energy Environ. Sci.*, 2019, **12**, 2548
Cu-SA/SNC	*Energy Environ. Sci.*, 2019, **12**, 3508
Fe/CoN-C	*Energy Environ. Sci.*, 2020, **13**, 3544
Fe_1/*d*-CN	*Energy Environ. Sci.*, 2021, **14**, 6455
4.2-FeSA	*Energy Environ. Sci.*, 2022, **15**, 1183
Fe/Zn-N-C	*Energy Environ. Sci.*, 2022, **15**, 1601
Fe-N,O/G	*Energy Environ. Sci.*, 2023, **16**, 2629
Fe_x-N@CF Fe_x/Cu-N@CF	*Energy Environ. Sci.*, 2023, **16**, 3576
As-DC1-1050	*Energy Environ. Sci.*, 2024, **17**, 123
Fe-N_4P/NPC Fe-N_4SP/NPS-HC	*Energy Environ. Sci.*, 2024, **17**, 249
ZnCoFe-TAC/NC ZnCoFe-TAC/SNC	*Energy Environ. Sci.*, 2024, **17**, 2298

References

1. H. Ogasawara, B. Brena, D. Nordlund, M. Nyberg, A. Pelmenschikov, L. G. M. Pettersson and A. Nilsson, *Phys. Rev. Lett.*, 2002, **89**, 276102.

2. S. Sakong and A. Groß, *J. Chem. Phys.*, 2018, **149**, 084705.

3. R. Subbaraman, D. Strmcnik, A. P. Paulikas, V. R. Stamenkovic and N. M. Markovic, *ChemPhysChem*, 2010, **11**, 2825–2833.

4. X. Zhao, X. Li, L. An, K. Iputera, J. Zhu, P. Gao, R.-S. Liu, Z. Peng, J. Yang and D. Wang, *Energy Environ. Sci.*, 2022, **15**, 1234–1242.

5. Y. Lum and J. W. Ager, *Energy Environ. Sci.*, 2018, **11**, 2935–2944.

6. E. L. Clark, C. Hahn, T. F. Jaramillo and A. T. Bell, *J. Am. Chem. Soc.*, 2017, **139**, 15848–15857.

7. W. Deng, P. Zhang, B. Seger and J. Gong, *Nat. Commun.*, 2022, **13**, 803.

8. M. Fekete, R. K. Hocking, S. L. Y. Chang, C. Italiano, A. F. Patti, F. Arena and L. Spiccia, *Energy Environ. Sci.*, 2013, **6**, 2222–2232.

9. L. Li, J. Zhou, X. Wang, J. Gracia, M. Valvidares, J. Ke, M. Fang, C. Shen, J. Chen, Y. Chang, C. Pao, S. Hsu, J. Lee, A. Ruotolo, Y. Chin, Z. Hu, X. Huang and Q. Shao, *Adv. Mater.*, 2023, **35**, 2302966.

10. J. Xu, D. Aili, Q. Li, E. Christensen, J. O. Jensen, W. Zhang, M. K. Hansen, G. Liu, X. Wang and N. J. Bjerrum, *Energy Environ. Sci.*, 2014, **7**, 820–830.

11. H. Li, S. Kelly, D. Guevarra, Z. Wang, Y. Wang, J. A. Haber, M. Anand, G. T. K. K. Gunasooriya, C. S. Abraham, S. Vijay, J. M. Gregoire and J. K. Nørskov, *Nat. Catal.*, 2021, **4**, 463–468.